

ALMA multi-band, multi-scale dust study of L1527

Evidence for (sub-)millimeter dust grains in the envelope of a Class I YSO

L. Cacciapuoti^{1,2,3}, L. Testi^{1,2,3}, E. Macias^{1,2,3}, A. Miotello^{1,2,3}, A. J. Maury³, Ł. Tychoniec¹, A. Natta, FauST, ECOGAL, and others

¹ European Southern Observatory, Karl-Schwarzschild-Strasse 2 D-85748 Garching bei Munchen, Germany

² somewhere

³ somewhere else

Received XX, 2022; accepted YY, 2022

ABSTRACT

Context. Protoplanetary discs around both young (class 0/I) and more evolved (class II) stars display substructures thought to be carved, among other effects, by planets. Class II discs, though, seem to show a lack of solid mass when compared to the known exoplanet population, as opposed to their younger counterparts. This deficit could be explained by the early conversion of small dust grains into large, undetectable planetesimals at Class 0 and I stages of stellar and disc formation. A potential early grain growth in protostellar envelopes in-falling on young discs has been suggested in recent studies, supporting the idea that solids start to agglomerate already during the Class 0/I phase.

Aim. We aim to indirectly determine the maximum dust grain size in the envelope of the Class 0/I source L1527, located in the Taurus star-forming region (140 pc). Probing grain sizes in the envelopes of such young objects is an ongoing quest, the findings of which might ultimately set the initial conditions of planetesimals formation.

Methods. We make treasure of Atacama Large Millimeter/sub-millimeter Array (ALMA) and Atacama Compact Array (ACA) archival data and present new observations, in an effort to both enhance the signal-to-noise ratio of the faint extended continuum emission and properly model the compact emission. Using observations performed in four bands and extending the spatial range of previous studies, we place tight constraints on the spectral and dust emissivity indices in a range of scales up to 3 times larger than what has been done in the recent past.

Results. We find $2.6 \leq \alpha \leq 3.0$ at all envelope scales (80-200 au in radii). The dust emissivity index $0.8 < \beta < 1.6$ shows a positive outwards gradient consistent with ISM-like grains at 2000 au and with the presence of (sub-)millimeter-sized dust grains in the inner envelope, where $\beta_{300\text{au}} = 1.00 \pm 0.06$. These findings are robust against possible caveats such as the assumed temperature profile of the envelope and the effects of chemical and physical composition of the dust. The low β suggests that either (sub-)millimeter grains have already grown at large (10^2 au) scales in the envelope of L1527, or they have been transported from the disc to the envelope, perhaps by its outflow.

Key words. planets and satellites: formation, protoplanetary discs

1. Introduction

Circumstellar discs orbiting Class II young stellar objects (YSOs) are also commonly referred to as *protoplanetary* discs even though a large fraction of them already displays structures thought to be shaped, among other effects, by embedded planets (Andrews et al. 2018). Rings, gaps and spirals have also been observed in younger ($<1\text{Myr}$) discs (ALMA Partnership et al. 2015, Sheehan & Eisner 2018, Segura-Cox et al. 2020, Nakatani et al. 2020). Several mechanisms have been proposed to explain the formation of structures in the early stages of the disc lifetime, such as gravitational instabilities (Takahashi & Inutsuka 2014); disc winds (Johansen et al. 2009, Takahashi & Muto 2018), the evolution of dust (Okuzumi et al. 2016). Among these, the early formation of pebbles and then large planetesimals that gravitationally interact with the disc remains a viable explanation.

Early formation of planetary embryos is also suggested by the dust mass budget of evolved discs when compared to their younger progenitors. Manara (2018) and Tychoniec et al. (2020) showed that the solid dust mass observed in evolved Class II discs of the Lupus star-forming-region seems to be 1-2 orders of

magnitude lower than the mass of known exoplanet population at that time. On the other hand, the Class 0/Is discs of Perseus contain roughly the same mass in solids as the known exoplanets do. While the recent findings of Mulders et al. (2021) suggest that the solid masses in Class II disks and exoplanets might be of the same order of magnitude. If planets start forming only in Class II discs, however, reconciling these results would require an unrealistic planet formation efficiency of 100%. One possible explanation is that the lacking mass might have been quickly converted into planetesimals. Direct observational evidence for kilometer-sized bodies remains undetectable for any radio interferometer and the problem remains open. Simulations that aim to reproduce the pathways to planet formation emphasize the importance on initial conditions, especially particle size (e.g., Ormel et al. 2009). In an effort to model planet formation at early stages (Class I), Cridland et al. (2022) find that replenishment of the disk material from the envelope sets favorable conditions for planet formation. However, medium to large grains ($> 30\mu\text{m}$) are required to meet the streaming instability conditions (Youdin & Goodman 2005).

An additional reason to investigate the properties of dust grains in these extended envelopes is to constrain the role that dust grains play as sites - and catalysts - of molecular reactions in diffuse environments. Indeed, although the most commonly accepted pathways to produce complex organic molecules in prestellar cores differ in several aspects, they all rely on the presence of icy mantles on dust grains to capture the building blocks of these complex molecules and facilitate reactions among them (e.g. Tielens & Hagen 1982).

One way to probe dust grain properties in protostellar environments relies on estimates of their spectral index α , the slope of the spectral energy distribution (SED) across (sub-)millimetric wavelengths. Specifically, if dust opacity scales as $\kappa \propto \nu^\beta$, in the optically thin regime and if the Rayleigh-Jeans (RJ) approximation holds, $\beta = \alpha - 2$ (Natta et al. 2007). Typical spectral indices for the interstellar medium - $\beta \sim 1.7$ - correspond to grain sizes in the range $100 \text{ \AA} - 0.3 \text{ }\mu\text{m}$ (Weingartner & Draine 2001). On the other hand, $\beta < 1$ has been observed in Class II objects, suggesting the presence of larger grains ($a \geq 1 \text{ }\mu\text{m}$) in more evolved discs (Testi et al. 2014).

However, the two assumptions that would allow to determine β as $\alpha - 2$ simply do not always hold. It has become clear in recent years that circumstellar discs can be optically thick even at millimeter wavelengths (Tazzari et al. 2021, Macías et al. 2021, Ueda et al. 2022). The correction for optically thick emission is even more important in young Class 0/I sources, where (i) the discs are partially obscured by the envelope along some lines of sight and (ii) resolving the two components separately is no easy task. Observations at more than two wavelengths are thus key to characterize the optical depth of the source throughout the involved physical scales, and critical to more robustly measure the spectral index. Moreover, the RJ approximation might not be valid for temperatures as low as the ones found in the outskirts of protostellar envelopes at given frequencies. Thus, even once α has been carefully measured, β has to be determined taking into account the departure from the RJ approximation (Mohanty et al. 2013).

In the recent past, several works have attempted to measure the dust emissivity index β at the large scales of Class 0/I protostellar envelopes to constrain whether dust growth might be significant at these very early stages of star and planet formation. Many have found surprisingly low β values (≤ 1) and interpreted this result as evidence for early dust growth (Kwon et al. 2009, Chiang et al. 2012, Miotello et al. 2014, Le Gouellec et al. 2019). Following similar methods, other works have not found hints of such growth (Agurto-Gangas et al. 2019). In their sample study of ten CALYPSO (Maury et al. 2019) Class 0 sources, Galametz et al. (2019) found examples of both relatively low and large β values.

Despite some of these findings, the hypothesis of early grain growth in the envelopes of Class 0/Is has been considered to be challenging from a theoretical perspective: growth to millimeter-sized particles seem to require environments characterized by higher density and longer timescales than the average Class 0 envelope (e.g. Ormel et al. 2009, Lebreuilly et al. 2022, Silsbee et al. 2022). These authors, using both analytical models and numerical simulations, find that particles cannot grow larger than $\sim 2 \text{ }\mu\text{m}$ in collapsing envelopes. Hence, while the mentioned observational works have played a major role in bringing this problem to light, it is now important to solve the remaining sources of uncertainty in their analysis: the limited sampling of the spatial and frequency ranges, the need for higher sensitivities to reduce the error bars on the spectral index of the faint envelopes, and

Table 1. Main properties of our target, L1527. References: [1] (Tobin et al. 2012); [2] (Karska et al. 2018); [3] (Motte & André 2001).

Alternative IDs	L1527 IRS, IRAS 04368+2557
RA	04h 39m 53.88s
Dec	+26° 03' 09.56''
Age [yrs]	$< 3 \cdot 10^5$ ^[1]
$M_* [M_\odot]$	0.2 ^[1]
$L_{bol} [L_\odot]$	1.6 ^[2]
$M_{4200au}^{env} [M_\odot]$	0.8 ^[3]

a robust modeling of the temperature profiles in the protostellar envelope.

Here, we focus on a single source in Taurus (140 pc), L1527. Due to its distance and brightness, L1527 is one of the most studied Class I to date. The presence of an edge-on circumstellar disc was first proposed by Tobin et al. (2010) with high-resolution $3.6 \text{ }\mu\text{m}$ Gemini-North observations and later confirmed by Tobin et al. (2013) with interferometric observations at 0.87 and 3.4 mm. The ALMA C^{18}O kinematic detection of the disc came in Ohashi et al. (2014) and Aso et al. (2017). Interestingly, the edge-on disc presents continuum asymmetries at $\sim 20 \text{ au}$ that are consistent with spiral structures, the physical origin of which has been proposed to be gravitational instability (Nakatani et al. 2020, Ohashi et al. 2022, Sheehan et al. 2022). Observations of L1527 also display prominent bipolar outflows extending to $20'000 \text{ au}$ perpendicular to the disc plane, and carving a cavity in the collapsing envelope (Tobin et al. 2010). L1527 represents an exceptional case in terms of data richness, thus providing a great opportunity to benchmark a dust continuum study of the envelope of a young protostar across several frequencies and physical scales.

In this paper, we aim to study the dust continuum emission of L1527 using the Atacama Large Millimeter/submillimeter Array (ALMA) and the Atacama Compact Array (ACA) to probe the outer (10^3 au) and inner (10^2 au) envelope, as well as the disc scales (10 au). We consider observations of our target in four different ALMA Bands (3, 4, 6, 7). Section 2 presents the ALMA and ACA observations that we have used throughout the analysis. Section 3 lays out the data reduction process. In Section 4, we justify the geometrical modeling used for the source in the uv-plane. In Section 5, we analyse the spectral and dust emissivity indices of L1527 at different scales. We discuss our results in Section 6 and wrap up our conclusions in Section 7.

2. ALMA observations

L1527 is one of the nearest Class I YSO, at approximately 140 pc in Taurus (Zucker et al. 2019): we summarize the details of our target in Table 1. This source has been extensively studied with both the Atacama Large Millimeter/submillimeter Array (ALMA) and the Atacama Compact Array (ACA). Archival data for this source comprehend high-resolution observations run to detect disc substructures as well as large-scale, high-sensitivity observations of the extended envelope aimed at characterizing its

Table 2. ALMA observations. For projects with more than one execution block, we only report the total integration time of the project. The rescaling factors are relative to the dataset whose factor is exactly 1.000.

Project Code	P.I.	Date	Integration (s)	Resolution	Frequency (GHz)	Rescale Factor	CASA version
Band 3							
2015.1.00261.S	Ceccarelli, C.	01/03/2016	3113	2"	85-87	0.93	4.5.2
		02/03/2016		2.4"	90-92	0.92	4.5.2
2016.1.01245.S	Cox, E.	04/01/2017	907	2.1"	99-114	1.06	4.7.0-1
2016.1.01541.S	Harsono, D.	21/12/2016	635	1.8"	92-105	1.14	4.7.0
2017.1.00509.S	Sakai, N.	14/11/2017	6150	0.09"	85-99	1.000	5.1.1-5
		14/11/2017		0.09"	85-99	1.04	5.1.1-5
		14/11/2017		0.09"	85-99	1.04	5.1.1-5
2018.1.01205.L	Yamamoto, S.	4/01/2017	1783	1.1"	93-108	-	5.6.1-8
Band 4							
2016.1.01203.S	Oya, Y.	19/11/2016	4697	0.8"	138-150	0.96	5.1.1
		03/09/2017		0.1"	138-150	0.92	5.1.1
2016.1.01541.S	Harsono, D.	10/03/2017	241	2.1"	144-154	0.97	4.7.0
		31/03/2017		2.1"	144-154	1.000	4.7.0
Band 6							
2012.1.00647.S	Ohashi, N.	20/07/2014	2117	0.4"	218-233	1.000	4.2.1
		20/07/2014		0.4"	218-233	1.01	4.2.1
2013.1.01086.S	Koyamatsu, S.	24/05/2015	2902	0.6"	219-234	0.85	4.5.0
		20/09/2015		0.2"	219-234	0.99	4.5.0
2013.1.00858.S	Sakai, N.	18/07/2015	2388	0.2"	245-263	0.96	4.4.0
2012.1.00193.S	Tobin, J.	11/08/2015	7348	0.2"	244-260	0.94	4.3.1
		02/09/2015		0.2"	244-260	1.05	4.3.1
2017.1.01413.S	van 't Hoff, M.	10/09/2018	968	0.3"	226-240	1.05	5.4.0
		28/09/2018		0.3"	226-240	1.07	5.4.0
2011.0.00604.S	Sakai, N.	10/08/2012	4838	0.6"	245-262	1.14	4.2.1
		26/08/2014		0.6"	245-262	1.09	4.2.1
2011.0.00210.S	Ohashi, N.	26/08/2012	1663	0.7"	219-231	1.05	4.2.1
2013.1.01331.S	Sakai, N.	02/02/2015	1209.6	1.2"	216-235	0.97	4.3.0
2018.1.01205.L	Yamamoto, S.	26/10/2018	1360.8	0.3"	244-262	1.10	5.6.1-8
		17/03/2019	362.0	1.1"	244-262	1.10	5.6.1-8
		15/12/2019		?	244-262	1.11	5.6.1-8
		26/10/2018	2358	0.3"	244-262	1.01	5.6.1-8
		07/03/2019	635.0	1.1"	244-262	1.004	5.6.1-8
Band 7							
2012.1.00346.S	Evans, N.	14/06/2014	635	0.3"	343-357	1.11	4.2.1
2015.1.01549.S	Ohashi, N.	26/07/2016	847	0.2"	329-341	1.000	4.5.3
2016.A.00011.S	Sakai, N.	29/07/2017	3592	0.075"	339-352	0.95	4.7.2
		05/09/2017		0.075"	339-352	1.01	4.7.2
2011.0.00604.S	Sakai, N.	29/08/2012	4233	0.5"	338-352	1.12	4.2.1

chemistry. We collected every available ALMA and ACA dataset suitable for our study of L1527, aiming to combine them in the deepest continuum analysis of its envelope so far. A summary of the datasets used in this work can be found in what follows and in Tables 2 and 3.

2.1. ALMA FAUST Band 3 & Band 6

Here, we present new B6 and B3 data from the ALMA Large Program *Fifty AU Study of the chemistry in the disk/envelope system of Solar-like protostars* (FAUST, PI: Satoshi, Y.; Codella et al. 2021). The observations were centred at $\alpha(2000) = 04^h39^m53.878s$, $\delta(2000) = +26^\circ03'09.56''$.

Band 3 data was collected on December 14th, 2018 and August 25th, 2019 with the 12m array in ALMA configurations C43-3 and C43-6, respectively. The baselines of these observations thus ranged 15-2500 meters. ALMA observed L1527 in the 93-95 and 104-108 GHz ranges with a spectral resolution of approximately 58 MHz. The source was observed for approximately 35 minutes in B3, for a continuum sensitivity of 0.025mJy

Band 6 observations were performed between October 20th, 2018 and December 15th, 2019 with both the 7m and 12m arrays. The baselines of the 7m array ranged from 8.9 to 48.9 meters. The 12m array observations were taken in configurations C43-2 and C43-5, with baselines ranging from 15-314 meters and 15-1400 meters, respectively. ALMA observed in the 244-247 and 258-262 GHz ranges with a spectral resolution of approximately 62.5 MHz. The source was observed for approximately 75 minutes in B6, for a continuum sensitivity of 0.026mJy.

The FAUST data were calibrated using a modified version of ALMA pipeline version 42866, using CASA 5.6.1-8. This included a correction for errors introduced by the per-channel normalization of data by the ALMA correlator¹. Line-free LSRK frequency ranges were identified by visual inspection and averaged per spectral window, and initial continuum images were produced for each separate ALMA configuration. These were then used as initial models for subsequent per-configuration phase-only self-calibration, followed by amplitude and phase self-calibration. Great care was used to ensure that the models

¹ <https://help.almascience.org/kb/articles/what-errors-could-originate-from-the-correlator-spectral-normalization-and-tsyst-calibration>

Table 3. ACA observations. The total integration times refer to the sum of the integration times within the entire project, in the cases with more than one execution block. The rescaling factors are relative to the 12m array dataset observed with the 12-m array, whose rescaling factor is 1.000 (cfr Table2).

Project Code	P.I.	Date	Integration (s)	Resolution	Frequency (GHz)	Rescaling Factor	CASA version
Band 3							
2016.1.01541.S	Harsono, D.	30/01/2018	907	13.0"	92-105	1.06	4.7.0
2018.1.00799.S	Pineda, J.	05/10/2018	5235	12.0"	92-107	1.06	5.4.0
		05/10/2020		12.0"	92-107	1.07	5.4.0
		06/10/2018		12.0"	92-107	1.05	5.4.0
		06/10/2018		12.0"	92-107	1.08	5.4.0
		06/10/2020		12.0"	92-107	1.06	5.4.0
Band 4							
2016.1.01541.S	Harsono, D.	27/10/2016	302	9.1"	144-154	1.07	4.7.0
2016.2.00171.S	Harsono, D.	24/08/2017	6168	7.8"	144-154	1.03	4.7.2
		03/09/2017		7.8"	144-154	1.01	4.7.2
		04/09/2017		7.8"	144-154	0.93	4.7.2
		12/09/2017		7.8"	144-154	0.99	4.7.2
Band 6							
2016.2.00117.S	Yoshida, K.	31/08/2017	26943	4.3"	230-245	1.12	4.7.2
		01/09/2017		4.3"	230-245	1.09	4.7.2
		15/09/2017		4.3"	225-245	1.11	4.7.2
		16/09/2017		4.3"	225-245	1.10	4.7.2
		16/09/2017		4.3"	225-245	1.02	4.7.2
		16/09/2017		4.3"	225-245	1.10	4.7.2
		17/09/2017		4.3"	225-245	1.03	4.7.2
		17/09/2017		4.3"	225-245	0.99	4.7.2
		17/09/2017		4.3"	225-245	0.95	4.7.2
2018.1.01205.L	Yamamoto, S.	24/10/2018	4474	5.9"	216-235	0.98	5.6.1-8
		20/10/2018		4.8"	245-262	1.07	5.6.1-8
Band 7							
2016.2.00117.S	Yoshida, K.	15/09/2018	2782	3.1"	352-363	1.15	4.7.2

were as complete as possible to avoid changing the overall flux density scale of the data when doing amplitude self-calibration. L1527 is sufficiently strong that per-integration phase-only self-calibration was possible, while for amplitude self-calibration per-scan self-cal was used. The per-configuration datasets were then aligned across configurations in both phase (to correct for any position offsets) and amplitude (to correct for any amplitude scale offsets), again using a self-calibration technique. Corrections to the amplitude scale of up to 10% were found to be needed for some datasets. Improvements in the dynamic range (peak/RMS away from emission) of more than an order of magnitude for the final images were achieved using this technique for setup 1 and 2. The improvement for setup 3 was $\sim 35\%$. Finally, we imaged the visibilities with the CASA *tclean* function, using the hogbom deconvolver, a 'briggs' weighting scheme with robust parameter set to 0.5. The resulting beam in B3 is $0.44'' \times 0.27''$ wide with PA= -29° ; while the synthesized beam in B6 is $0.42'' \times 0.28''$, PA= 19° . We present the new continuum maps in Fig. 1 and Fig. 2.

2.2. ALMA Band 3

We gathered ALMA Band 3 observations of L1527 spanning from 2017 to 2020. Given the different scientific aims of the projects, the data collected with the 12-m array has a resolution between $0.09''$ (project 2017.1.00509.S, PI: Sakai, N.) and $2.4''$ (project 2015.1.00261.S, PI: Ceccarelli, C.). The sensitivity of the 12-m array observations that have been used in this work ranges from 0.03 to 0.06 mJy and the total time on source is ~ 210 minutes. The frequency of the side bands ranges from 85 to 115 GHz.

The 7-m array has been pointed at L1527 in band 3 for a total

~ 102 minutes (projects: 2016.1.01541.S and 2018.1.00799.S; PIs: Harsono, D. and Pineda, J.). The observations have resolutions $12.0'' - 13.2''$ and have been carried out in a range of frequencies from 92 to 105 GHz with sensitivities of 0.3-0.6 mJy.

2.3. ALMA Band 4

L1527 has been observed in Band 4 throughout several months in 2016 and 2018. The data collected with the 12-m array has a resolution between $0.1''$ (project 2016.1.01203.S, PI: Oya, Y.) and $2.1''$ (project 2016.1.01541.S, PI: Harsono, D.). The sensitivity of the 12-m array data that have been used in this work ranges from 0.03 to 0.3 mJy and the total time on source is ~ 82 minutes. The frequency of the side bands ranges from 138 to 154 GHz.

The 7-m array observed L1527 in band 4 for a total ~ 107 minutes (projects: 2016.1.01541.S and 2016.2.00171.S; PI: Harsono, D.). The observations have resolutions $7.8'' - 9.1''$ and have been carried out in a range of frequencies from 144 to 154 GHz with sensitivities of 0.2-0.4 mJy.

2.4. ALMA Band 6

Band 6 observations of L1527 span from 2013 and 2020. The data collected with the 12-m array has a resolution between $0.2''$ (projects 2012.1.00193.S, 2013.1.00858.S and 2013.1.01086.S; PIs: Tobin, J.; Sakai, N. and Koyamatsu, S.) and $1.1''$ (project 2018.1.01205.L; PI: Yamamoto, S.). The sensitivity of the 12-m array observations that have been used in this work ranges from 0.03 to 0.09 mJy and the total time on source is ~ 403 minutes. The frequency of the side bands ranges from 218 to 263 GHz.

The 7-m array observed L1527 in band 6 for a total ~ 85 min-

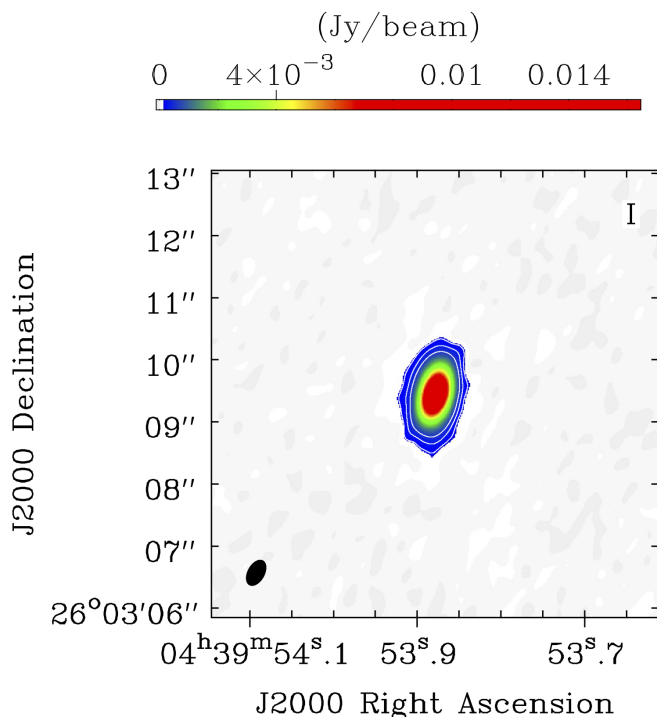


Fig. 1. Band 3 continuum of L1527 obtained with ALMA 12m array setups of the FAUST Large Program. The color map shows only flux densities higher than $\sim 5\sigma$, with the white contours highlighting the 5, 15, 30 σ levels. The ALMA synthesized beam is shown in black in the lower left corner.

utes. The observations have resolutions spanning $4.3'' - 5.9''$ (projects: 2016.2.00117.S and 2018.1.01205.L; PIs: Yoshida, K. and Yamamoto, S.) and have been carried out in a range of frequencies from 216 to 262 GHz with sensitivities of 0.4–1.0 mJy.

2.5. ALMA Band 7

L1527 has been observed in Band 7 from 2014 and 2018. The data collected with the 12-m array has a resolution between $0.075''$ (project: 2016.A.00011.S, PI: Sakai, N.) and $0.5''$ (project 2011.0.00604.S; PI: Sakai, N.). The sensitivity of the 12-m array observations that have been used in this work ranges from 0.06 to 0.2 mJy and the total time on source is ~ 155 minutes. The frequency of the side bands ranges from 218 to 263 GHz. The 7-m array observed L1527 in band 6 for a total ~ 46 minutes during project 2016.2.00117.S (PI: Yoshida, K.). The observations have resolutions $3.1''$ and have been carried out in a range of frequencies from 352 to 363 GHz with sensitivity of 1.44 mJy.

2.6. Data reduction and self-calibration

Since we worked with data taken at several frequencies, we avoid frequency smearing by splitting datasets with a relatively large frequency offset. This is especially important in Band 3, thus we split its datasets in two groups (cfr Fig.??). This way, after calibration, we will work on five final frequencies: 88, 100, 139, 241, and 342 GHz. These frequencies roughly correspond to 3.4, 3.0, 2.1, 1.2 and 0.88 mm wavelengths.

The first round of calibrations was performed using the standard CASA pipeline methods provided by the ALMA Regional Center (ARC). Considering the data we use was acquired over a several years period, different versions of the Common As-

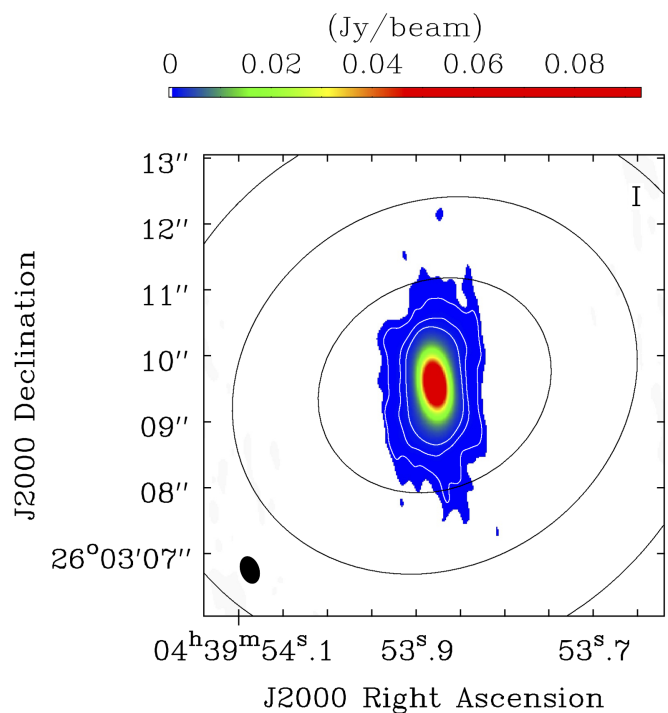


Fig. 2. Band 6 continuum of L1527 obtained by a combination of ALMA 7m and 12m arrays setups of the FAUST Large Program. The color map shows only flux densities higher than 7σ , with the white contours highlighting 10, 20, 40 σ levels. The synthesized beam is shown in black in the lower left corner. The [20, 40, 60] σ contours of the ACA-only image are overplotted in black. For clarity purposes, we omit the much larger beam of the latter.

tronomy Software Applications (CASA) (McMullin et al. 2007) were used. The version used for each dataset is listed in Table 2. This first round includes system temperature, phase, amplitude, and bandpass calibrations, along with corrections to account for atmospheric water vapor.

We carried out further data reduction and calibration steps and we used CASA version 6.2.1.7. First, the ALMA cubes for each execution block were inspected and additional flagging was applied when necessary, i.e. to mask out spectral lines. We are only interested in the continuum emission, thus, to speed up further operations, we channel-averaged the spectral windows of every execution block. We used a common width to level out the S/N among spectral windows and we were careful to avoid bandwidth smearing effects by limiting the averaging based on the maximum baselines and spectral window bandwidth (Bridle & Schwab 1999). Before combining the datasets for the analysis, we performed several additional operations. First, we imaged each averaged-channel visibilities with the *tclean* task and fitted a Gaussian with *imfit* to pinpoint the maximum of the emission, then we used the *fixvis* function to shift the phase center to the position of the peak of L1527 at the epoch of every observation. Since the target coordinates were slightly different across datasets, we also set the source sky position (in the metadata) to a common center across execution blocks using *fixplanets*. Once the coordinates of each dataset were phase-centered and aligned following this procedure, we rescaled the fluxes following the procedure of Andrews et al. (2018): for every frequency, we deprojected the real part of the visibilities, selected a range of uv-distances where the uv coverage of two datasets overlaps, binned the visibilities in that range, and compared them to obtain a re-scaling factor. The re-scaling factors were in a 1–15% range

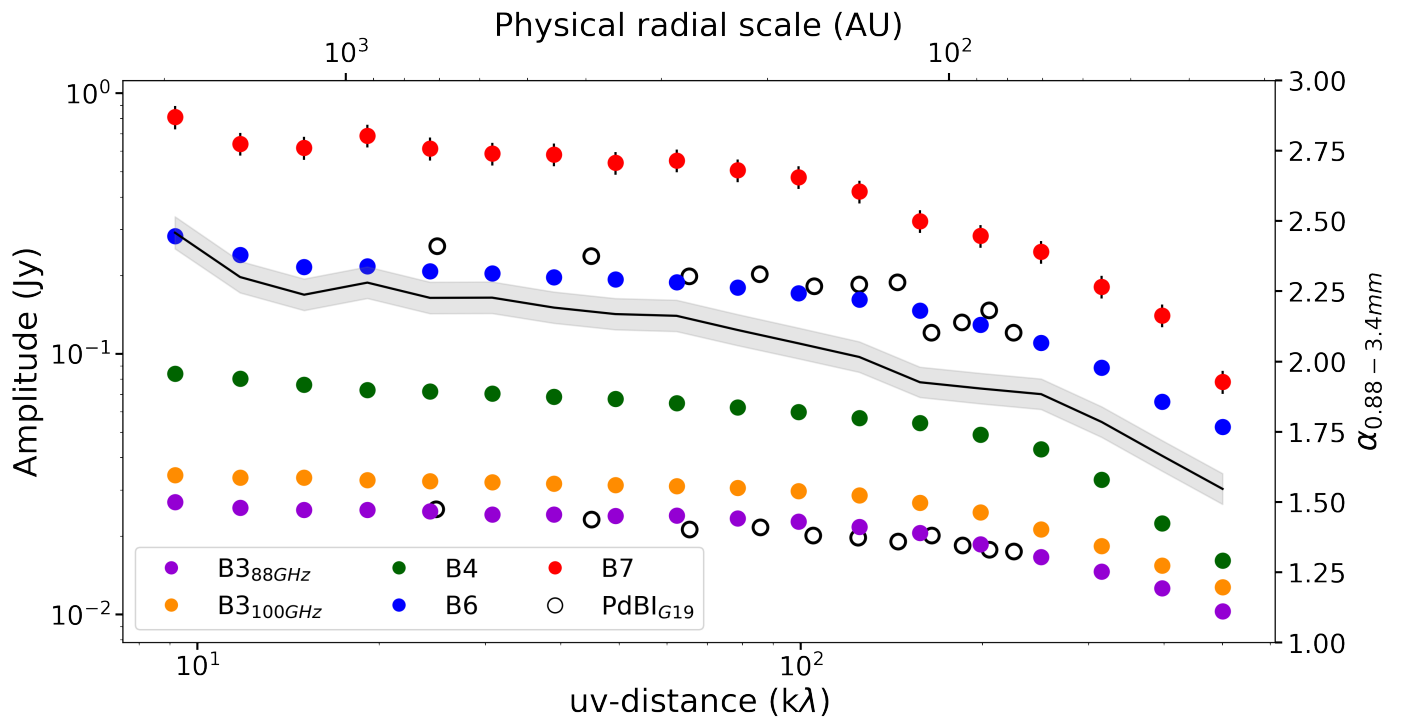


Fig. 3. Our L1527 ALMA 88 GHz (purple), 99 GHz (orange), 139 GHz (green), 241 GHz (blue), 342GHz (red) visibility amplitudes up to 1000 $k\lambda$. We also compare the 94 and 231 GHz observations (white points) performed with the Plateau de Bure Interferometer (PdBI) and analyzed in Galametz et al. (2019). The slope of our observed Spectral Energy Distribution (black line) has been obtained by fitting a line to the fluxes at all wavelengths in each uv-distance bin. While $1.5 < \alpha_{fit} < 2.5$, most of the contribution to the flux - and to α - at any uv-distance is due to the disc (see Section 4).

for all execution blocks. The re-scaling correction was then computed using the task *gencal* and the re-scaling itself was achieved by applying the correction factors with *applycal*. We report the rescaling factors in Tables 2 and 3.

We performed phase-only self-calibration to increase the signal-to-noise ratio (S/N) of our data, separately on each ALMA and ACA execution block. The starting S/N was high, in the range 20-900 across the different bands and measurement sets. For every different frequency and for each of the 7- and 12-meter arrays, we CLEANed a combination of all available measurement sets to create a first model. Based on this model, we then computed the phase corrections on each execution block using *gaincal* and applied them with *applycal*. This step aimed to correct phase errors between executions and between spectral windows. We repeated this procedure three times. In the first round, we set the solution interval of *gaincal* to *inf* and combine the scans within each execution block. In the second and third rounds, we combined the spectral windows of each block and shortened the solution interval. The self-calibration yielded peak S/N improvements in the range 10-500 % when evaluated on the images obtained with the combined datasets. We did not find any appreciable improvement in the noise and signal-to-noise properties for phase-only self-calibration steps with smaller time intervals. At this point, we combined the corrected datasets using the *concat* CASA task. Finally, we computed the weights on each new visibility point using *statwt*: this task calculates the variance of the real and imaginary parts separately and then uses their mean as the variance on the amplitude.

2.7. L1527 as seen in the visibility space

The final binned visibility amplitudes obtained with our data reduction and self-calibration are shown in Fig.3. We also show that the associated spectral index lies in the range $1.5 < \alpha_{0.88-3.4mm} < 2.4$. This low α is not surprising as the disc emission contribution dominates at every uv-distance (see Section 3), thus the total spectral index is strongly influenced by the optically thick disc (cfr. Section 4).

Among other Class 0s of the CALYPSO survey, the continuum emission of the envelope infalling on L1527 has been studied in Galametz et al. (2019) (hereafter, G19), who used PdBI observations at 1.3 and 3.2 millimeters. The data they used spans a range in uv-distances from 20 to 200 $k\lambda$ at both frequencies.

Fig. 3 shows a comparison between the ALMA observations we used and G19's PdBI fluxes. We cut the datasets at the shortest common baseline, set by Band 7 at 9.8 $k\lambda$. We aim to more robustly determine the spectral and dust-emissivity indices of the source by extending the frequency range, that dominates the error on α (see Section 4). Furthermore, a more dense sampling of frequencies is critical to understand the optical depth of the source across wavelengths, which is vital to constrain where the spectral index is a good proxy for dust grain sizes. On top of enriching the studied frequency range, we used a combination of ALMA and ACA data to study the dust continuum emission with high S/N at scales 2 times larger than G19, towards both shorter and longer baselines. In fact, although our primary attentions are devoted to the envelope, long-baseline visibilities are of great importance if we want to properly model the compact emission. G19 subtracted a constant amplitude ($F_{200k\lambda}$) from each visibility at the two frequencies, assuming a unresolved disc that would contribute a constant flux at baselines shorter than 200 $k\lambda$. Con-

sidering the wider uv-coverage of the data we used, we can more precisely model and subtract the compact emission by fitting a Gaussian component within a model that separately accounts for envelope and disc (see Section 3). This procedure also makes a significant difference when computing the errors on α and β , which in turn depend on the relative errors of the amplitudes. Since the PdBI amplitudes in G19 were roughly constant and only slightly above $F_{200k\lambda}$, the relative error on the fluxes after the subtraction of $F_{200k\lambda}$ became large already at a uv-distance of $\sim 100k\lambda$. Given the high S/N of our combined datasets, the relative flux uncertainty remains relatively contained after disc subtraction (see Fig. 6).

In the upcoming Section, we lay out the methods we followed to model the full visibilities and subtract the disc component to obtain an envelope-only spectral index.

3. Visibilities modeling

To investigate dust properties in the envelope of L1527, we worked in the visibility plane. This approach has two main advantages: 1) to keep the analysis clear of the artifacts and nonlinearities from which image reconstruction algorithms suffer; 2) when working with a large amount of interferometric datasets, it is not trivial to account for flux filtering in the imaged continuum maps across bands.

The visibility amplitudes are the combined flux of disc and envelope at all scales. Since we are mainly interested in studying the spectral index of the envelope, we have to disentangle the compact emission flux from the extended one. Hence, we fit the data in the visibility plane with a model that combines two profiles. Motte & André (2001) and Shirley et al. (2002) studied the protostellar envelopes of diverse Class 0/I YSOs and found power law density profiles with exponents in the $(-2.5, -1)$ range. Following their prescriptions, similarly to Maury et al. (2019), we consider a Plummer model (Plummer 1911) to be an adequate brightness profile of the protostellar envelope of L1527. In this model, the envelope's density is roughly constant inside a radius R_i while the outer envelope, $R > R_{out}$, has a density profile approaching a power law R^p , where p is a constant.

$$\rho(R) = \frac{\rho_i}{\left(1 + \left(\frac{R}{R_i}\right)^2\right)^{\frac{p}{2}}} \quad (1)$$

To obtain a brightness profile from the density profile, we need to combine the latter with a temperature profile for the envelope. Butner et al. (1990) derived the dust temperature distribution of a centrally heated power law envelope at radii $r > R_i$ to be a power law of radius and protostar luminosity:

$$T(R) = T_0 \left(\frac{R}{R_0}\right)^{-q} \left(\frac{L}{L_\odot}\right)^{q/2} \quad (2)$$

Equations 1 and 2 can be combined (Adams 1991) to obtain a Plummer-like intensity profile with which we can model interferometric visibilities:

$$I(R) = \frac{I_0}{\left(1 + \left(\frac{R'}{R_i}\right)^2\right)^{\frac{p+q-1}{2}}} \quad (3)$$

where R' is a projected radius. Finally, to account for the contribution of the protoplanetary disc, we sum a Gaussian component to Eq. 4, that we expect to better adapt our model to the

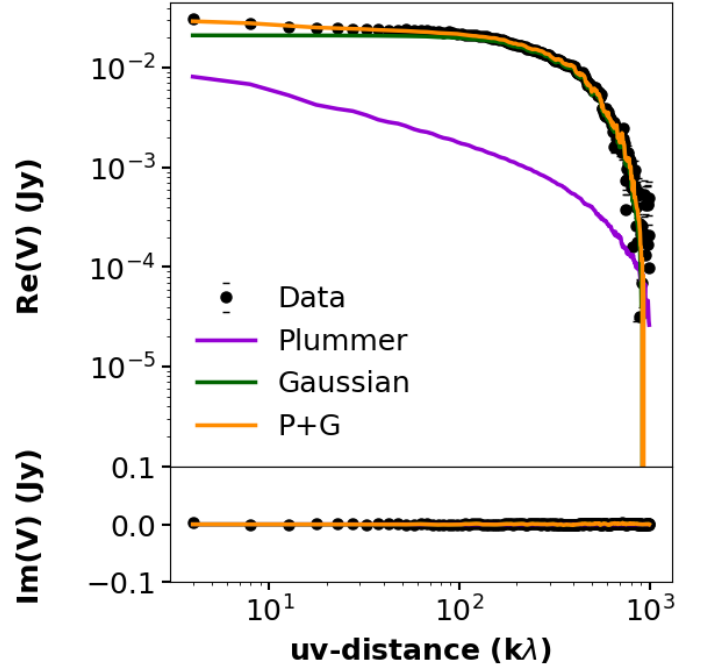


Fig. 4. The final Plummer+Gaussian best fit (orange) is overplotted on the data for Band 3 88 GHz (black points). The Plummer only (violet line) and Gaussian only (green line) components of the total model are also shown. In the case of the 88 GHz emission, the disc contributes up to 98% of the total emission.

data at long baselines:

$$I_{TOT}(R) = rI_0 \cdot e^{-\frac{R}{2\sigma^2}} + \frac{(1-r)I_0}{\left(1 + \left(\frac{R'}{R_i}\right)^2\right)^{\frac{p+q-1}{2}}} \quad (4)$$

The Gaussian is defined by a peak $f'_0 = rI_0$, a width σ , an inclination inc and position angle PA . The envelope power law has peak flux $f''_0 = (1-r)I_0$ and three free parameters: R_i , R_{out} , $(p+q)$. The peak fluxes of the extended and compact emission are modulated by the free parameter $0 < r < 1$. We have performed the fitting with *galario*, a library that exploits the power of modern graphical processing units (GPUs) to accelerate the analysis of observations from radio interferometers (Tazzari et al. 2018). In our framework, *galario* would compute a model image given our total profile, then it would Fourier-transform it into synthetic visibilities and sample them at the uv points covered by the antenna configurations with which the observations were performed. Then, it would run a minimum- χ^2 fit between the data and the model visibilities. The 10 fit parameters were the flux amplitude I_0 and the r factor; the width σ , the inclination (inc) and position angle (PA) of the Gaussian; the inner and outer envelope radii, R_{in} and R_{out} , and the power law exponent $(p+q)$. Finally two parameters, dRA and $dDec$, fit the offset of the peak from the phase center. For each fit, 60 walkers were set to run for 2,000 burn-in steps and 5,000 more steps after the burn-in stage.

The best fit results are summarized in Table 8. We show, as an example, the single best-fit model for the Band 3 88 GHz data, decomposed in its Plummer and Gaussian components (Fig. 4). We report the rest of the fits in Fig. 11, along with the best fit parameters summary (Table 8) in Appendix 8.

In particular, we find that the compact emission has a width of $0.15'' < \sigma_{fit} < 0.27''$ on the sky, depending on the Band. If we define the radius of the disc to be the 2σ contour of the

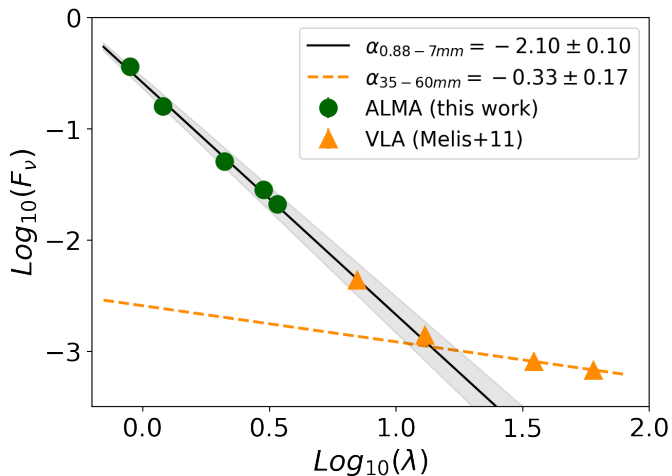


Fig. 5. The Spectral Energy Distribution of the circumstellar disc around L1527. Our *galario* best-fit total flux of the compact Gaussian component for each band, in violet, along with longer wavelength VLA measurements from Melis et al. (2011) and Sheehan & Eisner (2018). The 0.88-7mm spectral index computed using Sheehan et al. (2022) 7mm flux is consistent with optically thin emission, this difference might be due to a non-optimal subtraction of the non-thermal emission in this case, for lack of simultaneous longer wavelength measurements. The centimeter measurements of Melis et al. (2011) were taken quasi-simultaneously with respect to the rest of the observations. They constrain the free-free/synchrotron emission contribution using 3.5/6 cm fluxes.

Gaussian component, then $R_{disc} \sim 75au$ in Band 7, consistent with what was found in the kinematical analysis of Aso et al. (2017). In addition, the Gaussian component contributes to a minimum of 75% in B4, up to 98% in B3 (see Appendix 8 for the detail). While we fit the extended and compact emission self-consistently, we only use the best-fit parameters of the Gaussian components throughout our analysis. Indeed, we discuss the disc SED and the disc-corrected envelope emission SED in Section 4. For this reason, we don't discuss the envelope best-fit parameter here and we refer the reader to the Appendix, where we list the fitted parameters in Table 8.

4. Spectral and dust emissivity indices

If a circumstellar disc and its surrounding envelope are optically thin to the (sub-)millimetric radiation that their dust component emits after re-processing the absorbed starlight, and if this radiation is emitted in the Rayleigh-Jeans regime, the slope α of the SED yields information on the properties of the dust grains (Natta et al. 2007). Indeed, if the mentioned assumptions are satisfied, the dust opacity ($\kappa \propto \nu^\beta$) power law index is simply $\beta = \alpha - 2$.

In turn, β is dependent on dust grains properties such as the presence of an icy mantle, their chemical composition, porosity, and size. In this Section, we first derive the spectral indices of the observed emission at both disc and envelope scales, then we discuss to what extent these can be used to evaluate dust grain properties.

4.1. The circumstellar disc

To study possible early dust grain growth in the envelope of L1527, we made use of long baseline data to properly model the compact emission to be subtracted from the short baselines

amplitudes. In doing so, we obtained estimates of the flux of the compact ($0.15'' < \sigma_{fit} < 0.27''$) emission of L1527 in four ALMA bands. We here show the spectral energy distribution of the disc we obtained by combining and modeling all suitable ALMA archival data for L1527. To offer a more comprehensive view to the reader, we extended the range of wavelengths by including literature Very Large Array (VLA) measurements from Melis et al. (2011), up to 6 centimeters. Fitting the SED in the 0.88 to 7-millimeter range using our measurements along with the values of Melis et al. (2011), we find an optically thick disc with $\alpha = 2.1 \pm 0.1$. This is not surprising: the disc orbiting L1527 is very inclined ($i \sim 80^\circ$), almost edge-on in the sky: this geometric factor contributes to increase its optical depth along our line of sight. Furthermore, Ohashi et al. (2022) used high-resolution, multiple frequencies observations of the disc and found that the brightness temperature towards the mid-plane of the disc obtained by converting the flux at 0.88 mm ($\sim 42K$) is much lower than the ones found at 2 and 3 mm (60K and 90K, respectively). This progressive increase in brightness temperature means that the disc is at least partially optically thick at 0.88 and 2 mm. Since we do not observe a break in the SED in Fig.5, we deduce that the disc must be optically thick down to 7 millimeters. The high optical depth of the circumstellar disc of L1527 prevents us to conclude anything about its dust grain properties based on the spectral index. Finally, the 3.5 and 6 centimeters fluxes can be used to estimate the emission not due to thermal dust, that affects the measurements at all wavelengths. The slope at these longer wavelengths is $\alpha_{35-60} = 0.33 \pm 0.17$, as reported in Fig. 5 and is compatible with what is expected for free-free emission (Panagia & Felli 1975). However, it is worth noting that Melis et al. (2011) showed how the 3.5 cm flux of L1527 is highly varying in time. Indeed, they listed eight measurements (references therein) at this wavelength taken between 1996 and 2010 where the 3.5 cm flux shows significant variations between 0.55 and 0.81 mJy, with errors of the order of 1-5%. In Fig.5 we show Melis et al. (2011) points taken at roughly simultaneous epochs (2010 July 30th).

4.2. The envelope

We are now interested in investigating changes in the spectral index throughout the spatial scales of the envelope in the visibility plane. Starting from the common shortest baseline of $\sim 9k\lambda$, we log-uniformly bin the visibilities across the available uv-distances and then measure the spectral index in each bin. Since at this point we are interested in studying the spectral index of the envelope alone, we subtracted the *galario* best-fit Gaussian component of our model (see Section 3) from the data. This way, the remaining flux is the contribution of the extended emission only (Fig. 6).

Here, the amplitude $F = \sqrt{Re^2 + Im^2}$, and the error bars account for both statistical and calibration uncertainties. We set the latter to 10% for band 7 and 5% for bands 3, 4 and 6, following the prescriptions of the ALMA Handbook (Remjian et al. 2019). While the error on α is dominated by flux calibration errors on the observed amplitudes (see Fig.3), the relative amplitude error becomes important after the subtraction of the disc model. Not only the relative error is overall larger, it also visibly increases with uv-distance. This effect is clear in Fig.6 and Fig.10. Using almost every archival dataset for this source, we made an effort to maximize the S/N of the faint envelope of L1527 in what is its deepest continuum analysis.

To make the best use of our multi-wavelength data, we fitted a line to the fluxes along all wavelengths in each uv-distance bin

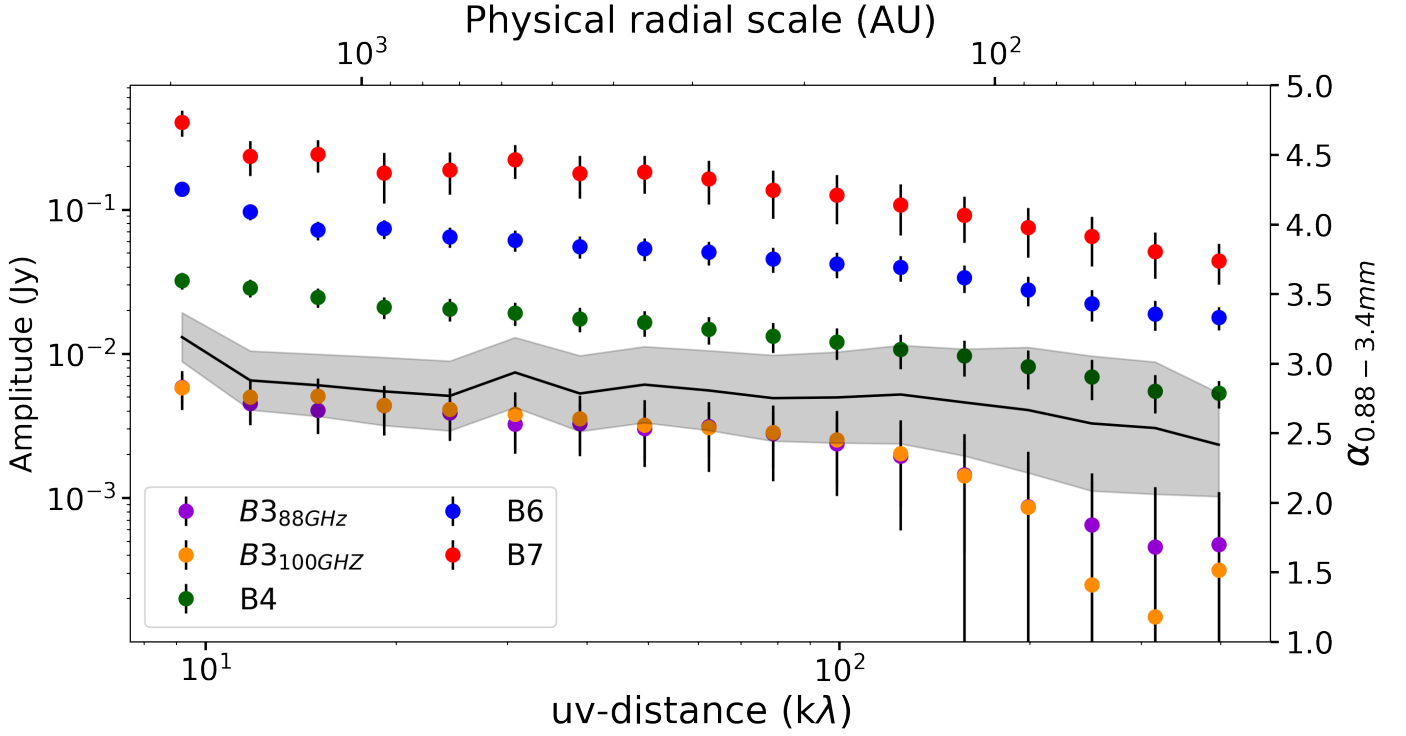


Fig. 6. L1527 ALMA band 3 (orange), 4 (green), 6 (blue), 7 (red) visibilities after removal of the fitted compact Gaussian component. The spectral index of the envelope emission (gray) has been obtained by fitting a line to the fluxes at all wavelengths in each uv-distance bin.

and we more robustly determined the spectral index. Since we combined a number of datasets for each band, the frequency of each flux point in each bin is taken to be the weighted average of the frequencies in that bin. The uncertainty on the spectral index obtained by fitting all bands is the error on the slope obtained with the weighted linear regression. Fig.6 shows that the fitted spectral index of the envelope of L1527 appears roughly flat in the studied range that spans from ~ 2000 down to 50 au, $2.6 < \alpha < 3.0$.

For completeness, we show the spectral indices computed between adjacent bands in Appendix 7. These are flat as well, although they show systematic differences in their average value, which clearly shows the need for a multi-frequency (>2) approach.

Finally, we measured the spectral index in different angle bins on the sky, after removal of the compact component. We divided the uv-plane into three different regions: the envelope ($-20^\circ < PA < 20^\circ$), the outflow ($70^\circ < PA < 110^\circ$) and the cavity walls (the remaining zones). We do not observe any significant difference among the three spectral indices at scales larger than 200 au Fig7.

4.3. $\beta_{env} \neq \alpha_{env} - 2$

The simple link between the spectral index α and the exponent of the dust opacity power law - $\alpha = \beta + 2$ - only holds for optically thin emission when the Rayleigh-Jeans approximation is valid. Thus, before interpreting the values of the envelope's spectral index in terms of dust properties, we check whether these necessary conditions are met, at the wavelengths we probe. First, we evaluate the optical thickness of the emission. The specific intensity I_λ , or flux per unit solid angle that we receive from the source (F_λ/Ω) can be generally expressed as an absorbed black

body:

$$I_\lambda = \frac{F_\lambda}{\Omega} = (1 - e^{-\tau}) \cdot B(T_{dust}) \quad (5)$$

where the optical depth τ modulates the difference between the observed flux F and the optically thick black body emission. If $\tau \ll 1$, then $F/\Omega \sim \tau B(T_{dust})$, while if $\tau \gg 1$, then the observed emission tends to a black body spectrum. Using the temperature prescription of Motte & André (2001) (cfr. Section 4.4), we find that, even at the shortest of our wavelengths, the envelope emission is optically thin at all scales as $F_{0.88mm}/\Omega < B(T_{dust})$ by a factor of 10 (see Fig. 8). The optically thin regime is naturally satisfied at longer wavelengths.

Secondly, we check if the RJ approximation is valid. Based on the same temperature profile for the dust, in the cold outskirts ($\sim 20K$ at 500 au) of the envelopes of such young discs, $h\nu/k_B T \sim 0.8$ at our mean B7 frequency of 342 GHz. This violates the RJ condition $h\nu/k_B T \ll 1$. Thus, while the envelope of L1527 is in the optically thin emission regime, it does not satisfy the RJ approximation and $\beta \neq \alpha - 2$. In the next Section, we derive the dust emissivity index using all available wavelengths but accounting for a correction due to the low envelope temperatures.

4.4. Dust emissivity index

Since we expect low temperatures in the envelopes of Class 0/I YSOs, for which the Rayleigh-Jeans approximation does not hold, we aim to determine β taking into account discrepancies from the $\alpha - 2$ proxy. First, we use the temperature profile of an envelope of optically thin dust and centrally illuminated by a protostar of luminosity L , as presented in Section 3. Butner et al. (1990) determined values for the free parameters q and T_0 of Eq. 2 via radiative transfer modeling of protostellar envelopes,

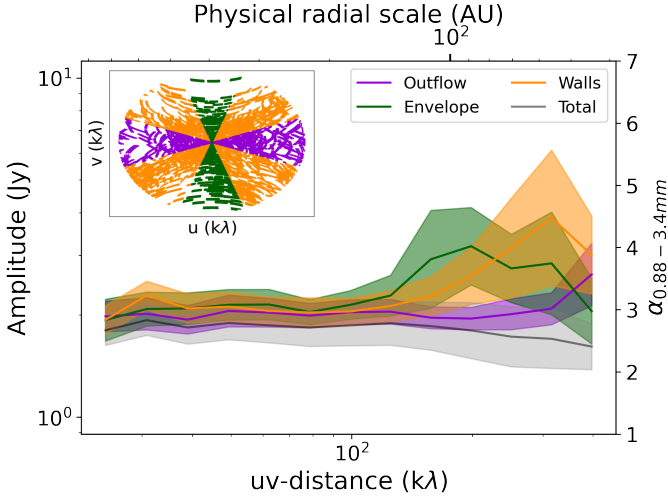


Fig. 7. The spectral index as measured along directions that correspond to the major (red) and minor (blue) axes of the L1527 disc, as well as the total α (black). The way the uv-coverage has been sampled is shown in the upper inset (B7 as an example). The scarce uv-coverage of the ACA Band 7 observations cause some bins to be undefined at the short baselines, hence the gaps in α .

obtaining:

$$T(R) = 38L^{0.2} \left(\frac{R}{100au} \right)^{-0.4} \quad (6)$$

Using this profile, β can be obtained as:

$$\log_{10} \left[\frac{F_\nu}{B_\nu(T)} \right] = \beta \cdot \log_{10} \nu + A \quad (7)$$

Considering this relation and the range of scales that we probe, the temperature gets as low as 10K in the outermost radii of the envelope ($\sim 1500 - 2000au$). Figure 9 shows how the dust emissivity index is nearly $\alpha - 2$ for the smaller spatial scales, where $T(R)$ is large enough, while it starts to show discrepancies after 200 au (where $T \sim 25K$). This temperature model is in agreement with the findings of Flores-Rivera et al. (2021), who used N_2H^+ and ^{12}CO Combined Array for Research in Millimeter-wave Astronomy (CARMA) observations along with $C^{18}O$ ALMA observations to perform radiative transfer modelling of the envelope of L1527.

The error on the dust emissivity index has been considered to be the same one that affects the spectral index since we are assuming an exact temperature profile, so $\Delta\alpha = \Delta\beta$.

In Figure 9, we report the measured β as a function of uv-distance, and we overplot a linear fit to the points, aiming to determine how the dust emissivity index changes when going from the inner envelope out to 2000 au. We find an increasing $0.8 < \beta < 1.6$ between 50 and 1500 au radial scales. We fit a line to the observed $\beta_{0.88-3.4mm}$ along the studied scales, and find:

$$\beta_{grad} = \beta(R_{au}) = (0.48 \pm 0.14) \cdot R_{au} - (0.18 \pm 0.46) \quad (8)$$

In turn, Eq. 8 yields:

$$\beta(R = 300au) = 1.00 \pm 0.06 \quad (9)$$

These estimates are consistent with the presence of (sub-)millimeter sized grains in the inner envelope of L1527.

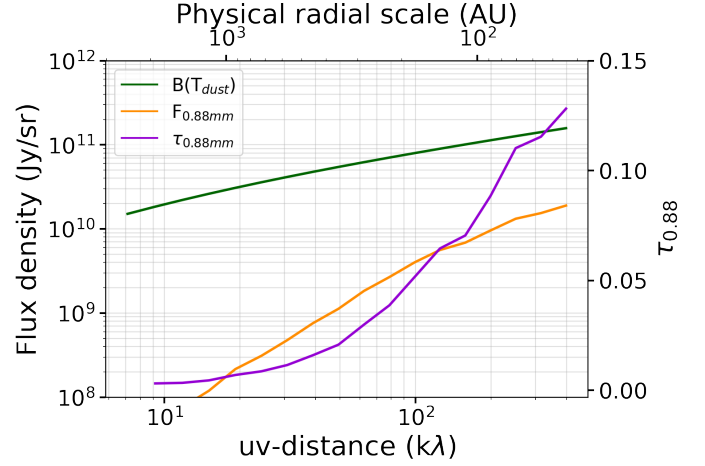


Fig. 8. The flux density of the envelope emission in ALMA Band 7 (orange) is consistently lower by at least an order of magnitude than a black body spectrum of emitting dust with a radial temperature profile $T \propto r^{-0.4}$ (green). The optical depth (violet) is much smaller than 1 at all envelope scales, thus we can consider the envelope emission at 0.88 mm as optically thin.

4.5. Literature comparison

Galametz et al. (2019) studied the envelope continuum emission of a few Class 0/I sources, among which L1527. Here, we compare our findings to theirs.

First, the wide uv-distance range of the datasets we used allowed us to model the disc emission, while only a constant amplitude was subtracted in the amplitudes in G19, who assumed an unresolved compact disc. This modeling is important to properly subtract the compact emission from the total amplitudes and work out the rest of the analysis on the flux of the envelope alone. Assuming the same temperature profile of G19 to compute the dust emissivity index, we find a different gradient and smaller uncertainties for β . These improvements have been obtained thanks to higher sensitivity data as well as the extension of the studied physical and frequency ranges. Firstly, G19 reported $\beta_{grad} = 0.18 \pm 0.39$. Noticeably, the flat β profile of G19 is consistent with what we observe across the same region they studied, 70-700 au radii. Extending the studied scale by a factor 2, we are able to explore the outer envelope and determine the positive outwards gradient of Eq. 8. The $\beta(R)$ thus derived is also consistent with typical ISM values at the outer scales (2000 au). Secondly, G19 reported a fitted $\beta_{500au} = 1.41 \pm 0.16$ while we find $\beta_{500au} = 1.16 \pm 0.05$ based on Eq. 7, reducing the error bar by a factor of three thanks to the extension we applied in frequency range.

5. Discussion

We argue that a multi-wavelength, multi-scale approach to study the envelopes of Class 0/I young stellar objects is a necessary step toward the understanding of the properties of dust grains therein. We made treasure of ALMA archival data of the borderline Class 0/I source L1527 in Taurus and found a roughly flat spectral index for the extended emission. After correction for departure from the Rayleigh-Jeans approximation due to the low temperatures in the envelope, we find a low dust emissivity index in the inner envelope scales. We now discuss our results as well as the caveats relevant to our analysis (Section 5.2).

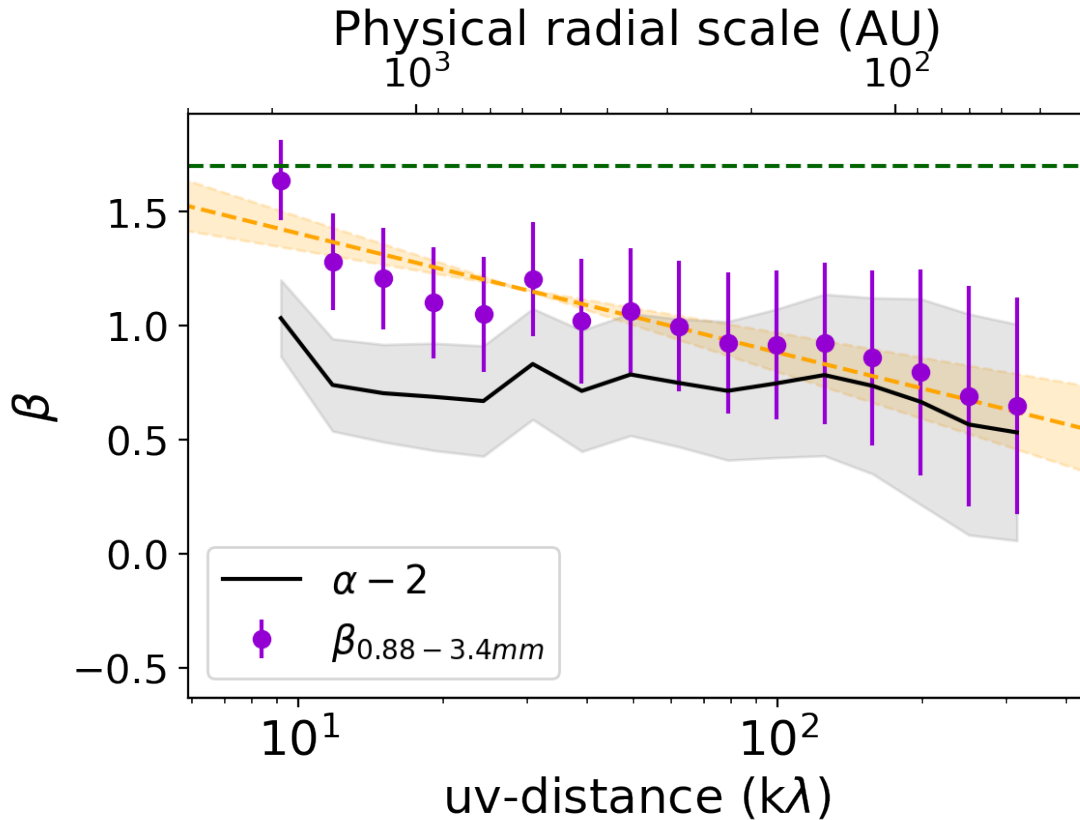


Fig. 9. Dust emissivity index (purple dots) of the envelope of L1527 as a function of physical scales. The solid dots indicate the β computed fitting all available bands. The dashed orange line is a linear fit to the solid dots. The black line shows the approximation in which $\beta = \alpha_{fit} - 2$, where α is the slope of the SED considering all five available frequencies.

5.1. Interpretations for $\beta \leq 1$ at $10^2 au$ scales

Given the low β values found at the large studied scales around L1527, we suggest that dust (sub-)millimeter grains could be present in the envelope of the Class 0/I YSOs L1527. If such solids grew in the envelope, this would have strong consequences on the way we think of the initial conditions for planet formation. However, a major problem arises in linking the observed low β with the presence of relatively large dust grains in a given environment. Indeed, theoretical studies of grain agglomeration have not been able to reproduce such growth in envelope-like environments. The numerical simulations of Ormel et al. (2009), Lebreuilly et al. (2022) and Bate (2022) have shown that it is very unlikely that solid dust grains could grow larger than about $1\mu m$ at the typical densities and timescales of envelopes such as the one in-falling on L1527 and its young disc. These authors included thorough treatment of grain-grain collision energetics, the effects of magnetic fields and relative grain velocities due to both turbulence and brownian motions.

On the other hand, Silsbee et al. (2022) proposed a simpler, analytical model to place strict upper bounds on the maximum grain size that can be reached in extended protostellar envelopes. They considered a coagulation model for the growth of spherical, yet fractal grains whose relative motions are driven by turbulence and the fragmentation of which happens for velocities above a quite generous threshold of $v_{rel} = 10m/s$. Considering that the optical properties of dust grains depended on the product of their radius (a) with a filling factor (or porosity) ϕ , they find that it is not possible to grow grains with an optical radius $a_{opt} = a\phi$ of 1 millimeter, in typical protostellar envelope condi-

tions. They find that, in the $10^5 yr$ s lifetime of a typical Class 0 source whose volume density is approximately $10^7 cm^{-3}$, grains grow up to about $2.5\mu m$.

While these theoretical works strongly disfavor the *in situ* production of (sub-)millimeter dust grains in the envelopes of young objects, the observational evidence of the low dust emissivity indices found therein remains largely uncontested. The main observational objection to the link between low β and large grains come from the dependency of the dust-emissivity index on other dust properties. In fact, the dust emissivity index is sensitive to changes in dust composition, porosity and the presence (or absence) of an icy mantle. Although variations in β are evident and well-characterized across different grain properties, Natta et al. (2007), Testi et al. (2014) and Köhler et al. (2015) concluded that $\beta < 1$ remains a strong evidence for the presence of (sub-)millimeter grains in the studied distribution. Additionally, Ysard et al. (2019) found that very few mineral mixtures can yield $\beta < 1$ for dust populations whose sizes peak at about $50\mu m$. These cases are represented by compact grains made of amorphous, carbonaceous material both with and without an icy mantle. The remaining models therein needed at least $a = 100\mu m$ to explain $\beta < 1$. Thus, although further laboratory studies will be necessary to understand which mixtures are more likely to populate these envelopes and to which β they would correspond to, dust particles larger than what expected for the typical ISM grains ($0.2 - 2\mu m$) still remain a perfectly viable explanation for our observational evidence.

If variations in the chemical and physical composition do not represent a robust alternative to large grains for explaining low dust emissivity indices, perhaps the temperature correction

discussed in Section 4.4 could be revisited. If the emission is optically thin, Equation 7 reduces to:

$$\beta = \alpha - \frac{d \log B_\nu(T)}{d \log \nu} \quad (10)$$

where the second term is 2 in case the Rayleigh-Jeans approximation is satisfied. The temperature power law we consider (cfr. Eq.2) yields temperatures of about 25 K at 200 au, where we find $\beta \lesssim 1$. Here, the correction term of Eq.10 amounts to 1.85. If the true temperature of the medium at 300 au were lower than what predicted with our simple power law, then the real β would be higher. However, to produce $\beta \sim 1.7$, the temperature of the envelope at 300 au would need to be lower than 5K, which is far below a reasonable value for a protostellar envelope.

Although simulations predict that large grains cannot grow *in situ*, observations strongly hint to their presence in the inner few hundreds au of these protostellar envelopes. A different mechanism that justifies their presence might be at play. Wong et al. (2016) proposed that such grains might be transported to the envelope after the growth has happened in the disc in the very early stages of the system. Their simple model suggested that a typical protostellar outflow ($T \sim 10\text{K}$, $v \sim 1\text{km/s}$) could lift grains as large as 1mm in the first 10^4yrs of the protostellar lifetime if the mass loss rate of the protostar was high enough ($\sim 10^{-6}\dot{M}_\odot/\text{yr}$). Furthermore, on the basis of three-dimensional magneto-hydrodynamical simulations, Lebreuilly et al. (2020) and Tsukamoto et al. (2021) found that the large dust grains grown in the inner region of a disk can be entrained by an outflow up to the envelope scales (up to a $100\mu\text{m}$ according to the former, and even $> 1\text{mm}$ for the latter). These grains then decouple from the gas and are ejected from the outflow into the envelope itself, enriching its dust population before falling back to the disc. While this is a fascinating scenario that would have implications for the meter-size barrier problem, the free-fall timescales of the dust back in the disc would make it extremely rare to observe such dust-enriched envelopes. Magnetic fields could play a critical role in sustaining the dust fall if the grains were charged, an eventuality that could be met in the lifting and ejection phases due to friction.

While a more thorough treatment of the link between the apparently large dust grains of L1527 and its envelope is outside of the scope of this work, we note that L1527 indeed hosts a large scale outflow structure in the East-West direction, i.e. perpendicular to the edge-on disc. Hogerheijde et al. (1998) observed the source with the James Clerk Maxwell Telescope and detected an outflow extending over about $20'000\text{ au}$ in the ^{12}CO ($J=3-2$) line emission. Moreover, Tobin et al. (2008) performed imaging of this source with the Gemini North telescope (in its L' band) and with the Infrared Array Camera (IRAC) on the Spitzer Space Telescope ($2.15\text{-}8.0\mu\text{m}$). They detected the outflow cavity up to roughly $10'000\text{ au}$ scale in both cases. Future investigations of whether or not this outflow could be the transport mechanism that entrained (sub-)millimeter grains from the inner L1527 disc to its envelope will be vital to understand the origin and effects of relatively large grains at such scales and evolutionary stage on planet formation models.

5.2. Caveats

Although we aim at presenting a more robust way of measuring the spectral index of the faint extended emission of the envelope of Class 0/I YSOs, our analysis is not free of caveats and more work will have to be done to further improve the reliability of our claims.

First, while we present a study of the spectral- and dust emissivity indices as a function of uv-distance and physical source scales, we have to keep in mind that a particular baseline does not only probe an annular region at some distance from the center, rather it probes any physical structure within a scale given by $\theta \sim \lambda/B$. It is for this reason that we have to model and subtract the disc from the visibility amplitudes before evaluating the spectral index for the envelope and, for the same reason, the α and β we compute for the envelope at different scales rather represent a flux-weighted average over the envelope spatial scales. If the inner envelope is much brighter than the outer one, as expected, the flux at even the shorter baselines is dominated by the inner envelope, thus the spectral index value at these scales would still be mainly describing the inner region. Indeed, our fitted power law shows that the envelope flux is 3 to 7 times smaller at the 500 au scales than it is at the 2000 au ones, depending on the band, with the largest gradients in B3 and B7.

Secondly, in Section 4 we have calculated the dust emissivity index β of the envelope taking into account discrepancies from the Rayleigh-Jeans approximation, hence accounting for a temperature profile, $T \propto r^{-0.4}$. This power law is the one of a dusty envelope illuminated by a central protostar (e.g. Terebey et al. 1993). While the values we obtain using this proportionality are reasonable as they don't reach values lower than typical cores temperatures at typical cores scales (10 K at 2000 au; e.g. Ferrière 2001), a more thorough treatment of the temperature structure and associated errors can be achieved by post-processing envelope models that well fit the data with radiative transfer simulations or by studying *thermometer* molecules in the envelope, like CH_3CCH .

For the moment, we relegate these refinements to a future study and wrap up our conclusions in the next Section.

6. Conclusions

We aim to characterize the maximum grain size of the dust distribution in the envelope of a Class 0/I YSO: L1527. Given its vicinity (140 pc), this source has been extensively studied over decades with different kinds of data and methodologies to investigate its star, extended envelope and circumstellar disc both in the dust continuum and line emission. In this context, we can make treasure of the richness of data from the Atacama Large (sub-)Millimeter Array to greatly enhance the S/N of the extended emission in the continuum and indirectly deduce the peak of the dust grains population in the envelope that surrounds and infalls the young circumstellar disc of L1527. We find that:

- The spectral index of the disc is $\alpha_{0.88-3.4\text{mm}} \sim 2$, consistent with the expected high optical depth of the edge-on disc of L1527. No dust grain properties information can be extracted in such a condition without thorough radiative transfer modeling, outside of the scope of this work.
- The dust emissivity index $0.8 < \beta_{0.88-3.4\text{mm}} < 1.6$ in the range of scales shown in Fig. 9 (70-2000 au). Such a low β in the inner envelope ($\beta_{300\text{au}} \sim 1$) can hardly be explained without the presence of large ($> 100\mu\text{m}$) dust grains. Furthermore, we find that the dust emissivity index shows a positive outwards gradient ($\beta(R) \sim 0.45R$) which hints to the presence of progressively larger grains from the very diffuse ISM-like environment down to the inner envelope.
- We discuss the implications of physical and chemical properties of dust grains on the values of β as well as the possible impact of the temperature profile used to calculate the correction for departure from the Rayleigh-Jeans approximation in

computing the dust emissivity index (cfr Section 5.1). None of these seem to be enough to justify values as low as 1 at hundreds of au, thus strengthening the hypothesis of (sub-)millimeter grains at these scales. While *in situ* formation seems disfavored by most theoretical studies, dust-transport mechanisms could have lifted such large grains the envelope of L1527, perhaps even its known outflow.

- We argue that a multiscale ($10^1 - 10^3$ au), multi-frequency ($n > 2$) and high-sensitivity study is necessary to tightly constrain the spectral- and dust emissivity index profiles. Using ALMA B3, B4, B6 and B7 effectively halves the error bars of measurements made in previous studies that made use of PdBI data, taken at two wavelengths only.

The Atacama Large Millimeter Array has provided us with necessary milestones in terms of resolution, recoverable scales, sensitivity and frequency ranges that are critical to the study of the continuum emission of faint, extended envelopes such as the one infalling on the young L1527. It is now the time to exploit this infrastructure to conduct sample studies of these objects with its state-of-the-art data to finally pinpoint the initial conditions of planet formation in both space and time.

Acknowledgements. This work was partly supported by the Italian Ministero dell'Istruzione, Università e Ricerca through the grant Progetti Premiali 2012-*i*ALMA (CUP C52I13000140001), by the Deutsche Forschungsgemeinschaft (DFG, German Research Foundation) - Ref no. 325594231 FOR 2634/2 TE 1024/2-1, by the DFG Cluster of Excellence Origins (www.origins-cluster.de). This project has received funding from the European Union's Horizon 2020 research and innovation program under the Marie Skłodowska-Curie grant agreement No 823823 (DUSTBUSTERS) and from the European Research Council (ERC) via the ERC Synergy Grant ECOGAL (grant 855130).

References

Adams, F. C. 1991, *ApJ*, 382, 544
 Agurto-Gangas, C., Pineda, J. E., Szűcs, L., et al. 2019, *A&A*, 623, A147
 ALMA Partnership, Brogan, C. L., Pérez, L. M., et al. 2015, *ApJ*, 808, L3
 Andrews, S. M., Huang, J., Pérez, L. M., et al. 2018, *ApJ*, 869, L41
 Aso, Y., Ohashi, N., Aikawa, Y., et al. 2017, *ApJ*, 849, 56
 Bate, M. R. 2022, *MNRAS*, 514, 2145
 Bridle, A. H. & Schwab, F. R. 1999, in *Astronomical Society of the Pacific Conference Series*, Vol. 180, *Synthesis Imaging in Radio Astronomy II*, ed. G. B. Taylor, C. L. Carilli, & R. A. Perley, 371
 Butner, H. M., Evans, Neal J., I., Harvey, P. M., et al. 1990, *ApJ*, 364, 164
 Chiang, H.-F., Looney, L. W., & Tobin, J. J. 2012, *ApJ*, 756, 168
 Codella, C., Ceccarelli, C., Chandler, C., et al. 2021, *Frontiers in Astronomy and Space Sciences*, 8, 227
 Cridland, A. J., Rosotti, G. P., Tabone, B., et al. 2022, *A&A*, 662, A90
 Ferrière, K. M. 2001, *Reviews of Modern Physics*, 73, 1031
 Flores-Rivera, L., Terebey, S., Willacy, K., et al. 2021, *ApJ*, 908, 108
 Galametz, M., Maury, A. J., Valdivia, V., et al. 2019, *A&A*, 632, A5
 Hogerheijde, M. R., van Dishoeck, E. F., Blake, G. A., & van Langevelde, H. J. 1998, *ApJ*, 502, 315
 Johansen, A., Youdin, A., & Klahr, H. 2009, *ApJ*, 697, 1269
 Karska, A., Kaufman, M. J., Kristensen, L. E., et al. 2018, *ApJS*, 235, 30
 Köhler, M., Ysard, N., & Jones, A. P. 2015, *A&A*, 579, A15
 Kwon, W., Looney, L. W., Mundy, L. G., Chiang, H.-F., & Kemball, A. J. 2009, *ApJ*, 696, 841
 Ladd, E. F., Adams, F. C., Casey, S., et al. 1991, *ApJ*, 382, 555
 Le Gouellec, V. J. M., Hull, C. L. H., Maury, A. J., et al. 2019, *ApJ*, 885, 106
 Lebreuilly, U., Commerçon, B., & Laibe, G. 2020, *A&A*, 641, A112
 Lebreuilly, U., Vallucci-Goy, V., Guillet, V., Lombart, M., & Marchand, P. 2022, *arXiv e-prints*, arXiv:2211.01891
 Macías, E., Guerra-Alvarado, O., Carrasco-González, C., et al. 2021, *A&A*, 648, A33
 Manara, C. F. 2018, in *Take a Closer Look*, 90
 Maury, A. J., André, P., Testi, L., et al. 2019, *A&A*, 621, A76
 McMullin, J. P., Waters, B., Schiebel, D., Young, W., & Golap, K. 2007, in *Astronomical Society of the Pacific Conference Series*, Vol. 376, *Astronomical Data Analysis Software and Systems XVI*, ed. R. A. Shaw, F. Hill, & D. J. Bell, 127
 Melis, C., Duchêne, G., Chomiuk, L., et al. 2011, *ApJ*, 739, L7

Miotello, A., Testi, L., Lodato, G., et al. 2014, *A&A*, 567, A32
 Mohanty, S., Greaves, J., Mortlock, D., et al. 2013, *ApJ*, 773, 168
 Motte, F. & André, P. 2001, *A&A*, 365, 440
 Mulders, G. D., Pascucci, I., Ciesla, F. J., & Fernandes, R. B. 2021, *ApJ*, 920, 66
 Nakatani, R., Liu, H. B., Ohashi, S., et al. 2020, *ApJ*, 895, L2
 Natta, A., Testi, L., Calvet, N., et al. 2007, in *Protostars and Planets V*, ed. B. Reipurth, D. Jewitt, & K. Keil, 767
 Ohashi, N., Saigo, K., Aso, Y., et al. 2014, *ApJ*, 796, 131
 Ohashi, S., Nakatani, R., Liu, H. B., et al. 2022, *ApJ*, 934, 163
 Okuzumi, S., Momose, M., Sirono, S.-i., Kobayashi, H., & Tanaka, H. 2016, *ApJ*, 821, 82
 Ormel, C. W., Paszun, D., Dominik, C., & Tielens, A. G. G. M. 2009, *A&A*, 502, 845
 Panagia, N. & Felli, M. 1975, *A&A*, 39, 1
 Plummer, H. C. 1911, *MNRAS*, 71, 460
 Remjian, A., Biggs, A., Cortes, P. A., et al. 2019, *ALMA Technical Handbook*, ALMA Doc. 7.3, ver. 1.1, 2019, *ALMA Technical Handbook*, ALMA Doc. 7.3, ver. 1.1 ISBN 978-3-923524-66-2
 Segura-Cox, D. M., Schmiedeke, A., Pineda, J. E., et al. 2020, *Nature*, 586, 228
 Sheehan, P. D. & Eisner, J. A. 2018, *ApJ*, 857, 18
 Sheehan, P. D., Tobin, J. J., Li, Z.-Y., et al. 2022, *ApJ*, 934, 95
 Shirley, Y. L., Evans, Neal J., I., & Rawlings, J. M. C. 2002, *ApJ*, 575, 337
 Silsbee, K., Akimkin, V., Ivlev, A. V., et al. 2022, *arXiv e-prints*, arXiv:2210.01832
 Takahashi, S. Z. & Inutsuka, S.-i. 2014, *ApJ*, 794, 55
 Takahashi, S. Z. & Muto, T. 2018, *ApJ*, 865, 102
 Tazzari, M., Beaujean, F., & Testi, L. 2018, *MNRAS*, 476, 4527
 Tazzari, M., Clarke, C. J., Testi, L., et al. 2021, *MNRAS*, 506, 2804
 Terebey, S., Chandler, C. J., & Andre, P. 1993, *ApJ*, 414, 759
 Testi, L., Birnstiel, T., Ricci, L., et al. 2014, in *Protostars and Planets VI*, ed. H. Beuther, R. S. Klessen, C. P. Dullemond, & T. Henning, 339
 Tielens, A. G. G. M. & Hagen, W. 1982, *A&A*, 114, 245
 Tobin, J. J., Hartmann, L., Calvet, N., & D'Alessio, P. 2008, *ApJ*, 679, 1364
 Tobin, J. J., Hartmann, L., Chiang, H.-F., et al. 2012, *Nature*, 492, 83
 Tobin, J. J., Hartmann, L., Chiang, H.-F., et al. 2013, *ApJ*, 771, 48
 Tobin, J. J., Hartmann, L., & Loinard, L. 2010, *ApJ*, 722, L12
 Tsukamoto, Y., Machida, M. N., & Inutsuka, S.-i. 2021, *ApJ*, 920, L35
 Tychoniec, Ł., Manara, C. F., Rosotti, G. P., et al. 2020, *A&A*, 640, A19
 Ueda, T., Kataoka, A., & Tsukagoshi, T. 2022, *ApJ*, 930, 56
 Weingartner, J. C. & Draine, B. T. 2001, *ApJ*, 548, 296
 Wong, Y. H. V., Hirashita, H., & Li, Z.-Y. 2016, *PASJ*, 68, 67
 Youdin, A. N. & Goodman, J. 2005, *ApJ*, 620, 459
 Ysard, N., Köhler, M., Jimenez-Serra, I., Jones, A. P., & Verstraete, L. 2019, *A&A*, 631, A88
 Zucker, C., Speagle, J. S., Schlafly, E. F., et al. 2019, *ApJ*, 879, 125

7. Adjacent bands spectral index

In this study, we have used multiple wavelengths to study the continuum emission of the envelope of L1527. This is critical to damp the possible systematic errors that occur when only using fluxes at two wavelengths. We show the importance of this approach in what follows. We computed α between adjacent bands (B7-B6, B6-B4, B4-B3) and between B3 and B6 (Fig. 10), as follows:

$$\alpha = \frac{\log_{10} F(\nu_2) - \log_{10} F(\nu_1)}{\log_{10} \nu_2 - \log_{10} \nu_1} \quad (11)$$

To evaluate the uncertainties on the spectral index between two wavelengths, we propagate the errors of Eq.11:

$$\Delta\alpha^2 = \left(\frac{1}{\ln\nu_2 - \ln\nu_1} \right)^2 \left(\frac{\sigma_1^2}{F_{\nu_1}^2} + \frac{\sigma_2^2}{F_{\nu_2}^2} \right) \quad (12)$$

where σ_1 and σ_2 are the uncertainties on the amplitudes in each uv-distance bin:

$$\sigma_i = \sqrt{\left(\frac{\partial F_i}{\partial Re_i} \right)^2 dRe_i^2 + \left(\frac{\partial F_i}{\partial Im_i} \right)^2 dIm_i^2 + \left(F_i \cdot dC \right)^2} \quad (13)$$

Here, Re and Im are the real and imaginary parts of the interferometric visibilities that make the amplitude as $F = \sqrt{(Re^2 + Im^2)}$,

and dC is the flux calibration error. We set the latter to 10% for band 7 and 5% for bands 3, 4 and 6, following the prescriptions of the ALMA Handbook (Remjian et al. 2019). In Figure 10, we show the spectral index of the envelope of L1527 as computed between adjacent bands, plus the one between B3 and B6. Fig. 10 shows how, given the statistical errors and the proximity of the adjacent bands, the error on α can be as large as 25% at the longest baselines. Moreover, the spectral index α shows slight systematic differences among different combination of adjacent bands. Only using multiple bands (>2), one can robustly constrain the spectral index, damping the uncertainties that arise using only two frequencies (see Section 4).

8. Fit results

As explained in Section 3, we fitted a composite model to the visibilities. The model comprehends a Gaussian component to trace the compact emission and a power law to better describe the extended emission. The disc radius, defined as the 2σ level of the Gaussian component is approximately 75 au in B7, consistent with what was found kinematically by Aso et al. (2017). The disc contributes to the flux from a minimum of 74% in B4 up to a maximum of 98% in B3 (100 GHz), supporting our choice to combine as many ALMA datasets as possible and selfcalibrate them in order to enhance the faint extended continuum emission. The disc results edge-on ($inc \sim 80^\circ$), consistently with several results throughout the literature with a position angle $PA \sim 2^\circ$, in a westward convention. The inner radius of the envelope is constrained to be in the range 0.01-0.15 arcseconds while the outer one is in the range 8-12 arcseconds, both depending on the band. Having phase-centered the datasets during the data calibration procedure, we find both dRA and dDec phase offsets consistent with zero. Finally, the power law exponent of the Plummer profile ($p + q$) is found to be in the range 2.6-3.2, roughly consistent with what was found by Ladd et al. (1991). We list the results of the fitting, that was carried out with *galario*, in Tab.8 and show the final model in Fig.11.

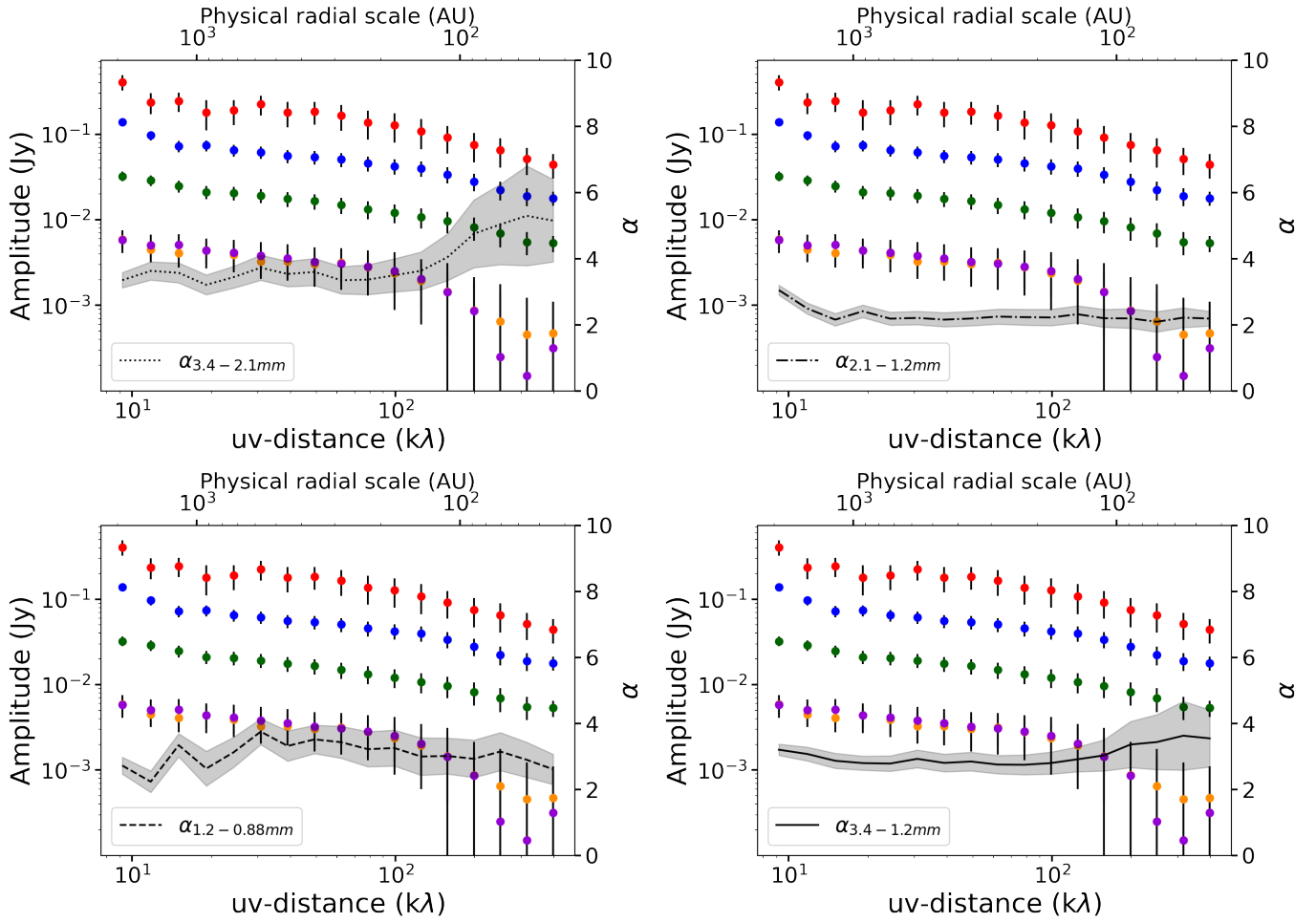


Fig. 10. L1527 envelope spectral index computed between adjacent bands only. The visibility amplitudes scale is on the left y-axis while the spectral index scale is on the right y-axis. The spectral indices computed only using adjacent bands show systematic offsets. A multi-wavelength study damps the uncertainty arising from this inconsistencies.

	Band 3 (88 GHz)	Band 3 (99GHz)	Band 4	Band 6	Band 7
f_0 (Jy/sr)	10.476 ± 0.002	10.526 ± 0.001	10.794 ± 0.003	10.9344 ± 0.0004	11.3847 ± 0.0001
r	0.892 ± 0.003	0.987 ± 0.001	0.743 ± 0.007	0.8559 ± 0.0003	0.8640 ± 0.0001
σ (")	0.1473 ± 0.0002	0.1513 ± 0.0002	0.2079 ± 0.0004	0.2781 ± 0.0001	0.26076 ± 0.00006
inc (deg)	80.001 ± 0.002	80.001 ± 0.001	80.002 ± 0.001	80.000 ± 0.002	80.000000 ± 0.000006
PA (deg)	2.08 ± 0.6	2.27 ± 0.02	2.04 ± 0.05	0.76 ± 0.01	1.942 ± 0.007
R_{in} (")	0.0292 ± 0.0005	0.144 ± 0.01	0.038 ± 0.001	0.14127 ± 0.00007	0.13730 ± 0.00005
R_{out} (")	9.97 ± 0.03	9.99 ± 0.01	12.8 ± 0.1	7.73 ± 0.04	9.9736 ± 0.0002
$p + q$	2.621 ± 0.009	2.76 ± 0.03	2.748 ± 0.005	3.178 ± 0.001	2.843 ± 0.001
dRA (")	0.02921 ± 0.00008	0.02946 ± 0.00007	0.0074 ± 0.0001	0.06736 ± 0.00003	0.00047 ± 0.00001
dDec (")	-0.0181 ± 0.0001	-0.01889 ± 0.00008	-0.0112 ± 0.0003	-0.04402 ± 0.00005	0.00458 ± 0.00003

Table 4. The galario best-fit parameters of the Gaussian+Plummer model, for each ALMA Band.

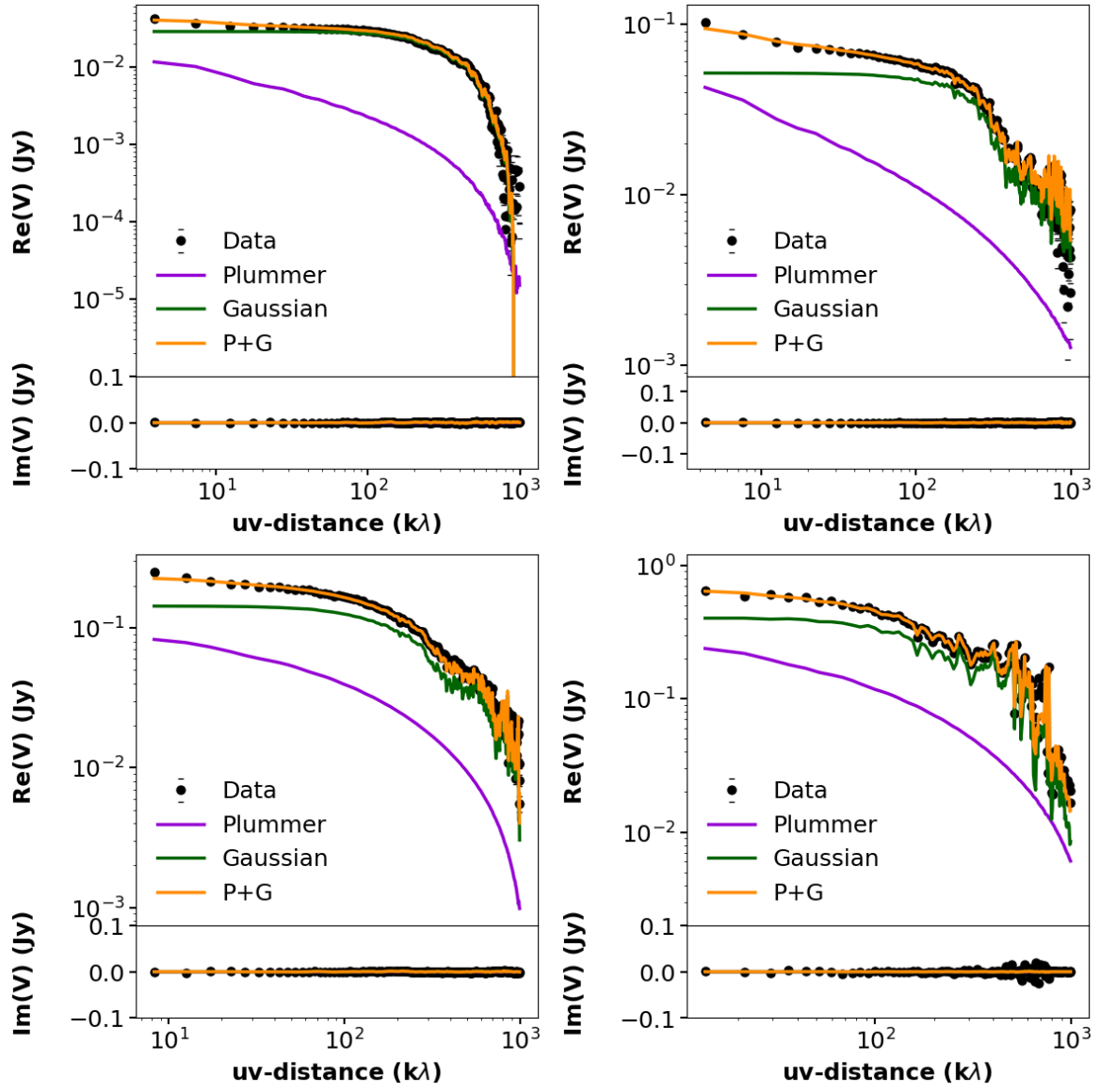


Fig. 11. The final Plummer+Gaussian best fit (orange) is overplotted on the data for Band 3 100 GHz (upper left), Band 4 (upper right), Band 6 (lower left), Band 7 (lower right). The Plummer only and Gaussian only components of the total model are shown in violet and green, respectively.